Astron. Astrophys. 341, 527–538 (1999)

ASTRONOMY AND ASTROPHYSICS

Evidence for large-scale, global mass inflow and flaring on the late-type fast rotator BD+22°4409

M.T. Eibe[1,⋆], P.B. Byrne[1], R.D. Jeffries[2], and A.G. Gunn[3]

[1] Armagh Observatory, College Hill, Armagh BT61 9DG, Ireland
[2] Department of Physics, Keele University, Staffordshire ST5 5BG, UK
[3] University of Manchester, Nuffield Radio Astronomy Laboratories, Jodrell Bank, Macclesfield, Cheshire, SK11 9Dl, UK

Received 27 April 1998 / Accepted 21 October 1998

Abstract. We present new results from high-resolution spectroscopic observations of the late-type fast rotator BD+22°4409, revealing interesting aspects about its magnetic activity that have not been considered before. Analysis of the extremely variable and rotationally broadened chromospheric Hα emission profile provides clear evidence for an intense and continuous downflow of absorbing material. A high level of activity was also exhibited in the form of two consecutive flares that lasted for almost five hours. The decay of the second flare was accompanied by a dramatic absorption in the blue half of the Hα profile that is attributed to the development of cool flare loops. The observed circulation of material and the presence of magnetic loops in connection to the chromospheric flare suggest plasma is being effectively transferred between the chromosphere and the corona.

As opposed to similar active and fast rotators, direct evidence of cool prominence clouds has not been found in this star. The results provide strong support for recent theoretical studies by van den Oord et al. (1997). In that work it was concluded that such prominences are only stable at some distance from the star in the equatorial plane. Unstable material would be expected to flow towards the poles along magnetic lines. The inclination of BD+22°4409, $i \sim 50^\circ$, favours the detection of such flow as an asymmetry in chromospheric lines profiles. However, it could make clouds undetectable if they can never be seen in projection on the disk.

Key words: stars: activity – stars: chromospheres – stars: individual: BD+22°4409 – stars: late-type

1. Introduction

Solar magnetic activity is believed to originate in a dynamo process, resulting from the coupling between convection and differential rotation. It manifests itself in a wide range of observable phenomena including flares, spots, plages, chromospheric network, prominences, etc.

Solar prominences are structures made of condensed cool matter suspended in the corona by magnetic fields. Prominence-like activity has also been observed in RS CVn binary systems (Hall & Ramsey 1992), although this is not a defining characteristic of the group (Gunn & Doyle 1997; Gunn et al. 1997). Recent observations have suggested that an analogue of solar prominences may be an ubiquituous phenomenon in late-type rapid rotators. Cool clouds of neutral material forced to corotate with the underlying star by its magnetic field have been detected in the K dwarf AB Dor (Cameron and Robinson 1989a,b), several G dwarfs in the αPer cluster (Collier-Cameron & Woods 1992), the active K dwarf HD 197890 (Jeffries 1993), the active M dwarf HK Aqr (Byrne et al. 1996, hereafter BER96) and the active M dwarf RE 1816+541 (Eibe 1998), all fast rotators. The characteristic dimensions and heights of these structures are considerably larger than solar prominences. It is well known that the degree of magnetic activity in rapidly rotating late-type stars is higher than in the Sun, due to the higher rotation rates and deeper convective regions.

The distribution of rotational velocity with age in cool dwarfs implies spin-down time-scales for rapidly-rotating stars that are too short to be explained by the classical theory for angular momentum loss. In the classical scenario, rotational braking occurs as a result of the interaction between a stellar wind and the ambient coronal field, as it is believed to occur on the Sun. The rotational velocity is expected to decrease monotonically according to the power law, $v\sin i \propto t^{-\frac{1}{2}}$ (Skumanich 1972). Recent studies of stellar rotation in a number of nearby open clusters (Stauffer et al. 1984, 1985; Stauffer & Soderblom 1991, and references therein) demonstrates that a more rapid braking mechanism must be introduced in order to justify the observed spin-down time-scales for G-type rapid rotators. In addition, such a mechanism must be dependent on mass in order to explain the longer time-scales that are observed for lower mass stars.

The presence of co-rotating prominences in rapid rotators could account for an additional loss of angular momentum as suggested by Cameron & Robinson (1989a,b). Therefore, it is important to determine how common this phenomenon is, to estimate the amount of mass involved and to derive cloud heights above the stellar surface in order to confirm the significance of its associated angular momentum.

Send offprint requests to: M.T. Eibe
⋆ *Present address:* LAEFF, Apdo 50727, E-28080 Madrid, Spain

Prominence clouds can be detected spectroscopically because they resonantly scatter the underlying chromospheric radiation out of the line of sight, producing transient absorption features in the rotationally broadened chromospheric Hα line profile. Since the clouds are forced to corotate with the star by their containing magnetic field, these transients move rapidly across the line profile with monotonically increasing radial velocities resulting in a systematic variability of the Hα emission. This effect repeats each time a cloud crosses the observer's line of sight in front of the stellar disk.

The star BD +22°4409 has been selected as a possible candidate for prominence activity. Previous observations of this star (Jeffries et al. 1994, hereafter J94) showed it to be a single K5-K7 dwarf with a projected rotational velocity $v\sin i \simeq 69\,\mathrm{km\,s^{-1}}$. The most probable period as determined from photometric data was found to be 10.17±0.10hr, which, in combination with an assumed main sequence radius for a star of its spectral type, yields an axial inclination of 50°±10°. Flaring and plage activity were detected but no convincing evidence of prominence-like structures was found. A possible geometric explanation was proposed at the time, related to the fact that co-rotating cool prominences may be impossible to detect in projection on the stellar disk in this particular case because of the low inclination of this star, i.e. that clouds occur only close to the equatorial plane. This view is further reinforced by recent modeling work of van den Oord et al. (1997).

In the following section we describe new observations of this star. Details of the analysis of the data, together with its results are contained in Sect. 3. In Sect. 4 we discuss possible interpretations for the various sources of chromospheric emission variability that have been identified in this system. Finally, the conclusions are summarized in Sect. 5.

2. Observations and data reduction

The observations were collected with the 4.2m William Herschel Telescope (WHT) at the Observatorio del Roque de los Muchachos on the island of La Palma, Canary Islands, on two nights, viz. 4 and 5 August 1993. The telescope was equipped with the Utrecht Echelle Spectrograph (UES, Unger et al. 1993) which, in combination with a 1242×1152 pixel EEV CCD detector yielded spectra at a resolving power of $\lambda/\Delta\lambda$=49 000 (FWHM) over the wavelength region 4500-7150 Å. Because of the placing of the detector with respect to the echellogramme, wavelength coverage was incomplete. Spectral gaps of about 19% occured at the red end of the range, decreasing to the blue, where complete coverage was achieved from 4500 Å. Exposure times were typically 200s, with a dead time of 100s due to chip readout, making an effective cycle time of 5min. A log of the data will be found in Table 1.

Spectra were flat fielded and bias corrected, wavelength calibrated and extracted from the echellogrammes using standard routines within the astronomical computing environment IRAF (Tody et al. 1986) on the STARLINK (Bromage 1984) computers at Armagh Observatory.

Table 1. Log of the spectroscopic observations of BD+22°4409 taken with the WHT/UES 4-5 August 1993. The start and end times of continuous sequences of spectra are recorded. The series were interrupted in order to take thorium-argon arc lamp exposures or correct autoguide errors. These gaps were normally not larger than 3min. Phases (φ) have all been referred to the first exposure of the object and were calculated using the period of 10.17hr (J94)

Date	JD (2449200+)		Phase	
	start	end	start	end
4 August	4.4252	4.5024	0.000	0.182
	4.5086	4.5856	0.197	0.378
	4.5954	4.6663	0.401	0.569
	4.6722	4.6952	0.582	0.637
5 August	5.3866	5.4900	0.363	0.537
	5.4936	5.5715	0.551	0.732
	5.5755	5.6698	0.745	0.962
	5.6734	5.7071	0.976	0.051
	5.7110	5.7280	0.073	0.101
	5.7320	5.7399	0.109	0.119

3. Determination of the stellar velocity

3.1. Radial velocity

The single photospheric line Fe I 6546.25 Å, well detected above the noise level, was chosen to obtain a first estimation of the stellar radial velocity. This line was fitted with a Gaussian function in all the individual spectra. From the average Doppler shift of the line a heliocentric velocity $v_{hel}\sim$–14 km s^{-1}±2 km s^{-1} was derived. The error, obtained as a standard deviation, indicates significant changes, larger than expected for a single star and for this spectral resolution.

Radial velocities obtained from Gaussian fits to photospheric lines can be uncertain due to asymmetries and/or blending with weaker lines. Therefore, a cross-correlation analysis was performed on a high signal-to-noise spectrum of the object, obtained from an average of several consecutive spectra. Gl820A, a non-active slowly rotating dwarf with a similar spectral type (K5) to that of BD+22°4409, was used as a template. The heliocentric radial velocity, computed from the shift of the cross-correlation peak, is v_{hel}=–18.13±5.08 km s^{-1}. Significant variations were found in both nights. Intrinsic differences between the star and the template may also contribute to the error. J94 obtained a similar result after cross-correlation with several radial velocity standards. The mean heliocentric velocity reported in their work was –17.4 km s^{-1}±2.3 km s^{-1}. For the remainder of the paper, we adopted the most precise of our measurements, –14±2 km s^{-1}, derived from the Gaussian fitting procedure described above.

In order to examine in detail radial velocity variations the same cross-correlation technique was applied to each individual spectrum in different orders. Results are shown in Fig. 1. It is clear that radial velocity variations are phase dependent and appear to be sinusoidal at the rotational period. The amplitude of the modulation is larger on the night of August 5 (*filled circles*). We disregard the possibility that the observed variations are due

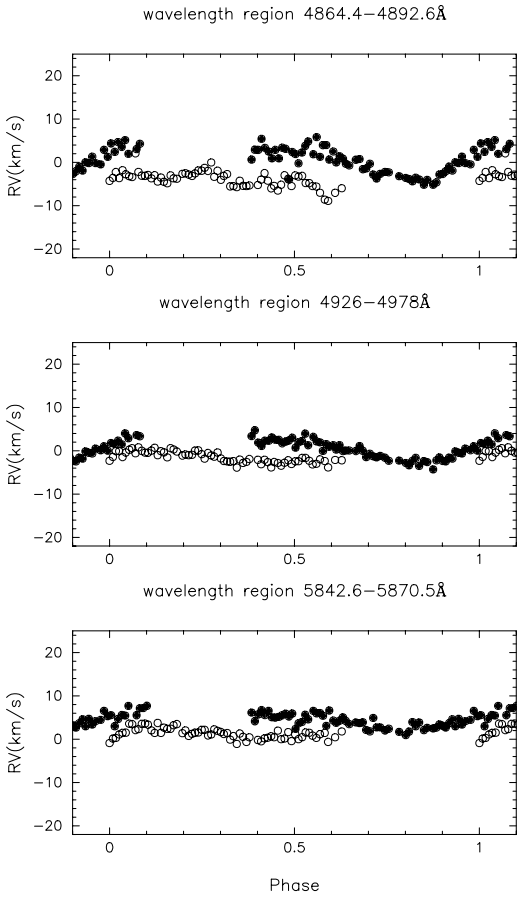

Fig. 1. Radial velocity variations with phase on the two nights, August 4 (*open circles*) and August 5 (*filled circles*). Velocities were determined from cross correlation of the spectra with respect to the spectrum of Gl 820A using the wavelength regions indicated on the top of the diagrams

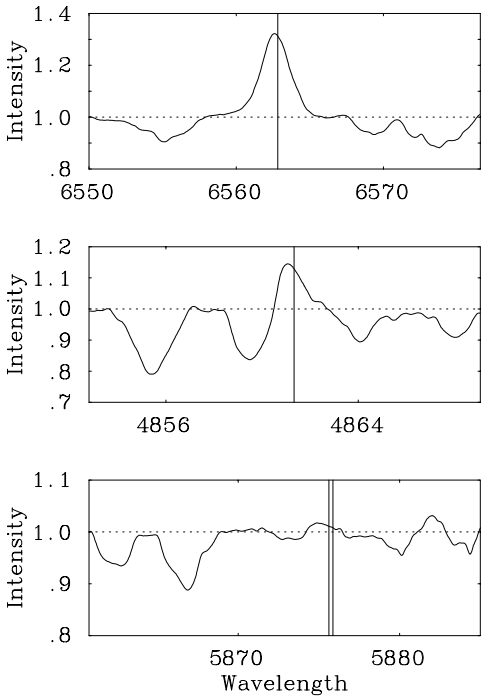

Fig. 2. The overall mean spectrum of BD+22°4409 based on the entire two nights' data in the vicinity of Hα (*upper panel*), Hβ (*middle panel*) and the He I D_3 doublet (*lower panel*). Note that the spectra were shifted to the rest wavelength of the star's photospheric spectrum before averaging, as described in the text. The *vertical lines* indicates the rest wavelength of each line while the horizontal dotted lines indicate the normalization level. Note the asymmetry of the emission in all three lines towards the blue

to an instrumental effect since calibration errors are not significant. Cross-correlation of arc lamp exposures taken throughout the night shows that wavelength calibration shifts could not be larger than $3\,\mathrm{km\,s^{-1}}$. Even these have been removed to first order by using calibration arcs close to the time of observation.

3.2. Rotational velocity

The rotational velocity was also determined from cross-correlation analysis of the spectra with respect to the spectrum of Gl 820A. A relationship between the width of the cross-correlation peak and $v\sin i$ was established by broadening artificially the template spectrum to a set of velocities. The synthetic rotational spectra were then cross-correlated with the unbroadened template spectrum. Least-squares linear fits were done to the pairs width-velocity function, providing the calibration needed to convert the measured width to rotational velocity. This method gives $v\sin i \simeq 68 \pm 2\,\mathrm{km\,s^{-1}}$. The error is a propagation of uncertainties in the calibration fit. This result is consistent with that of J94, $v\sin i \simeq 69 \pm 1\,\mathrm{km\,s^{-1}}$, obtained by using a similar procedure.

4. Chromospheric lines

The computed radial velocity was used to correct all the spectra so that they were finally referred to the rest velocity of the photosphere. An overall mean spectrum in the region of the Hα, Hβ and He I D_3 chromospheric lines, based on both nights' data, is shown in Fig. 2.

Both Balmer lines are strongly in emission, as would be expected for an active late-type star, while He I D_3 is also in emission but weak. An interesting result is the apparent asymmetry of the emission features, in the sense that emission is mainly seen to the blue side of the rest wavelength. In view of previous evidence of Hα variations in similar rapidly rotating late-type active stars we now examine evidence for the same kind of related variations in BD+22°4409.

4.1. Hα variability

Even casual examination of sequences of spectra clearly shows that the Hα line is variable. In order to quantify this we have proceeded initially as in BER96. Individual normalized line profiles were fitted with a single gaussian, so that the variability could be represented by means of the temporal evolution of three main parameters of the fits, i.e. the wavelength of the line centre, λ_0, the equivalent width, EW, and the full width at half maximum,

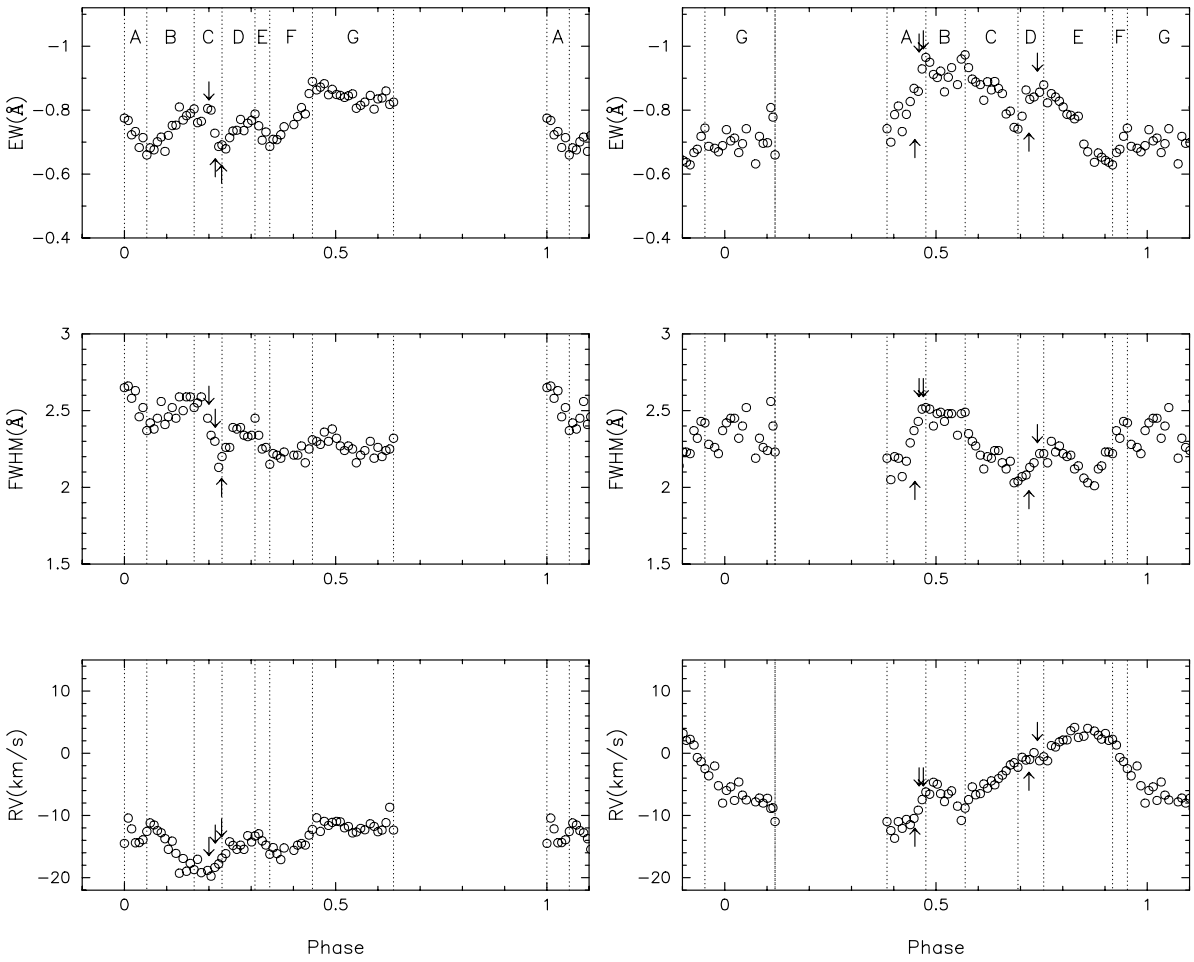

Fig. 3. Evolution of the gaussian parameters derived from fits to the Hα line profile during the night of August 4^{th} (*left*) and the night of August 5^{th} (*right*), as explained in Sect. 4.1. Phases have been calculated by defining the time of the first exposure on the first night as zero and using the rotational period, P=10.17hr (J94). The dotted vertical lines divide the plots into sections according to significant changes in the slope of the EW. Each interval of phases is labeled to help their identification in the text. The small arrows indicate the times at which He I D_3 emission was detected

FWHM. The results are shown in Fig. 3. Vertical dotted lines divide the plots in sections to distinguish the main changes that take place during each night, generally defined by an alteration of the slope of the EW evolution. Note that, following the usual (but not universal) convention, negative EW indicates that the line is in emission but in the text we will refer only to the absolute values. The RV parameter plotted in Fig. 3 is the Doppler velocity corresponding to the wavelength shift of the Hα line centre from its wavelength in the rest frame of the star.

On August 4 the EW exhibits rapid variations during intervals A–F, with peak-to-peak amplitudes of the order $\sim$0.15 Å($\sim$20%) on time scales corresponding to phase intervals, $\Delta\varphi \sim$0.05–0.1. However, after $\phi \sim 0.45$ the $\mathrm{EW_G}$ reaches a plateau $\simeq$0.84 Å. The FWHM appears to vary in a similar way although individual changes are less marked.

The temporal evolution of RV (Fig. 3, *left*) is related to that of EW and FWHM in the sense that the main changes occur almost simultaneously. The detailed relationship between RV and the other two parameters is less readily discerned. For instance, whereas the evolution towards a minimum velocity at ϕ = 0.2 corresponds to an increase of both EW and FWHM, the next blueshift, at $\phi \simeq$0.37, is accompanied by a *decline* in the EW and FWHM.

On August 5 the EW variability is more extreme than in the previous night and is characterized by two consecutive peaks. The first peak (interval B) is the highest ($\overline{\mathrm{EW}}_{\mathrm{B}} \sim$0.92 Å) and lasts for $\Delta\phi \simeq$0.31. The second peak (intervals D–E), with $\mathrm{EW}_{max} \simeq$0.88 Å, extends over a shorter interval of phase, $\Delta\phi \simeq$0.18. As on the first night, FWHM generally correlates well with EW.

The RV has a sinusoidal appearance with total amplitude $\simeq$25 km s^{-1}. A marked positive deviation from this otherwise smooth trend takes place at B, coinciding with the peak in both EW and FWHM. There is another slight deviation at D but in a blueward direction.

We note that, during those phases where the two nights overlap, there is reasonable but not exact agreement between the behaviour of the gaussian parameters.

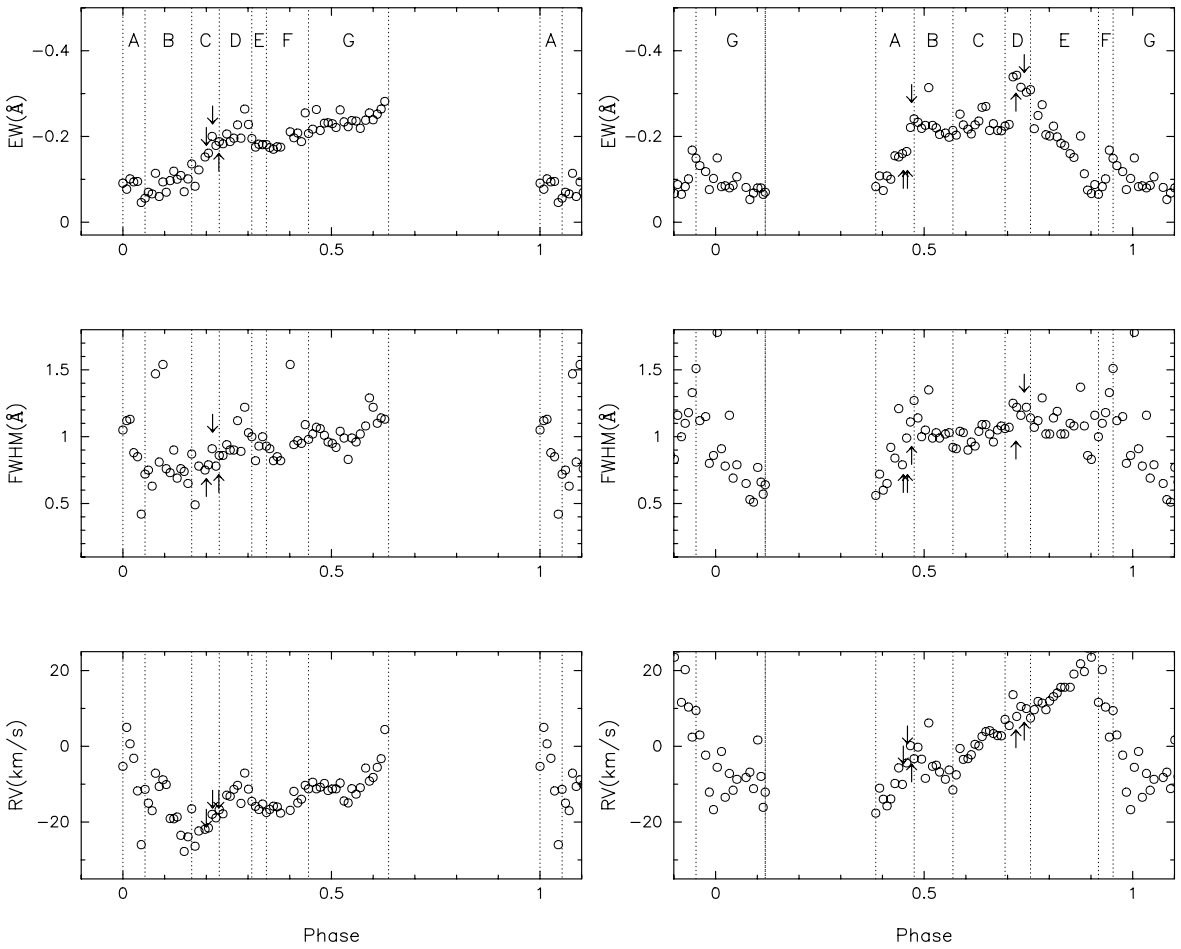

Fig. 4. Temporal evolution of the main gaussian parameters derived from the fits to the Hβ line profile during the night of August 4^{th} (*left*) and the night of August 5^{th} (*right*). Details of the plots are as in Fig. 3

4.2. Hβ variability

Since Hβ is an intrinsically much weaker line, the signal-to-noise of the Hβ profiles is much less than for Hα. In order to aid comparison with Hα we have applied the same analysis to the Hβ profiles. The results are shown in Fig. 4. The intervals of phase used in Sect. 4.1 are retained here. Results are very scattered compared to Hα, making a detailed comparison very difficult.

Some differences in the Hβ behaviour on August 4 can be seen in Fig. 4 (*left*). The peak of $EW^{(H_\alpha)}$ in B does not exist in Hβ and only the peak at interval D is seen clearly in the two lines. In addition, $EW_G^{(H_\beta)}$ is almost constant as observed in Hα. On the other hand, the general trend in RV(Hβ) is consistent with RV(Hα), although absolute values are different.

As in Hα, the most important features of EW and FWHM variability on August 5 (Fig. 4, *right*) are the two large increases seen at intervals A and D, respectively. The peak in interval D is in fact better distinguished in Hβ. Another sharp increase occurs in F, which is less marked in Hα. On the other hand, G is an interval of relative constancy in both lines.

On this night, the Hβ line centre varies by a relatively larger amount and more symmetrically with respect to zero than Hα. This is especially marked in $RV_{E–F}$. The total amplitude of the variations is $\simeq$30 km s^{-1}. Deviations from the general trend are again seen in intervals B and perhaps D. This reproduces the behaviour observed in Hα in a general way but there are important differences of detail. We note at this point that the lack of detailed agreement in RV between Hα and Hβ supports an interpretation in terms of absorption rather than chromospheric mass motions as discussed later (see Sect. 8.1).

As seen in Hα the general trends are consistent between the two nights with differences only in detail especially in the RV curves near $\varphi \simeq 0.5$.

5. Investigation of variable components in the Hα profile

We first address the issue of the large asymmetry of the mean observed emission profiles (see Sect. 3). The expected FWHM of a spectral line in the Hα region from a star rotating at $v \simeq 69$ km s^{-1} in the absence of limb-darkening is at least 2.61 Å. This is a reasonable approximation for a chromospheric line like Hα since the bulk of the observed flux arises over a thin layer of uniform emissivity with depth. The observed mean FWHM is 2.3 Å, substantially less. The Hβ line, which is formed at a deeper layer in the chromosphere, shows a similar asymme-

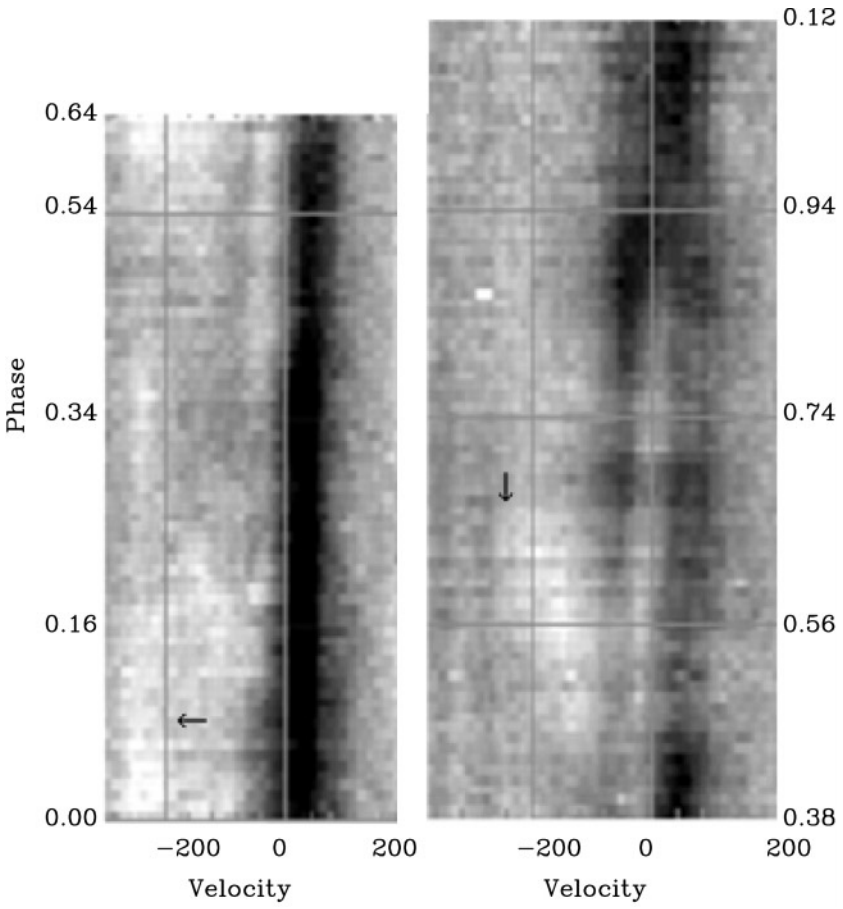

Fig. 5. Grey-scale images displaying the ratio spectra for the observations of August 4 (*left*) and August 5 (*right*). Rows are individual Hα profiles after division by the reference profile (see Sect. 5), placed in chronological order from bottom to top. The velocity scale in the horizontal axis is referred to the stellar rest frame. The small arrows indicate excess emission in the blue wing, which is discussed in the text.

try. This would suggest the effect is caused by a circumstellar source rather than by surface inhomogeneities. Otherwise more disagreement would be expected between asymmetries in Hα and Hβ, since the limb-darkening coefficients are different in both lines. The time-averaged Hα profiles should have a FWHM at least as big as the Doppler width, so it seems reasonable to assume that they are absorbed in the red over a substantial part of the star. On the other hand, if the absorption was localized on the stellar surface it should move on the profile with rotation. The analysis presented in Sect. 4, however, suggests its effect is not exactly uniform with phase.

In order to investigate possible variations of this asymmetry we examined in detail the Hα profiles by comparison to a reference spectrum. We first made an average of several Hα line spectra taken on the first night, selected so that they were not affected by significant variability. Their phases are marked in Fig. 3 (*left panel*) as interval G. Next the blue wing of the average spectrum was reflected to the red with respect to the Hα rest wavelength. The resulting profile has a FWHM of 2.6 Å, which agrees well with the value predicted from the $v\sin i$. It seems reasonable therefore to assume that such a profile would correspond to that of an uniform chromosphere for this star. We used it as a reference to investigate the nature of the variations seen in Figs. 3 and 4.

The individual spectra were divided by the reference template and the resulting ratio profiles stored in a 2-dimensional array for each night. Fig. 5 shows the results as grey-scale images, which will be referred to as *dynamic ratio spectra*. Each line of an image corresponds to a single ratio profile with time running from bottom to top.

As can be seen in Fig. 5 (*left*), the general appearance of the Hα profiles on August 4 is dominated by a strong absorption in the red at all phases, being especially dense during $\phi \sim$0.0-0.4, i.e. intervals A–F in Fig. 3. This effect is slightly attenuated at the end of the night (interval G in Fig. 3). The general trend of the variations is complicated by the sudden appearance of variable emission in the blue wing with velocities of the order of –200 km s^{-1} ($\varphi \sim$0–0.2 and $\varphi \sim$0.6). Its behaviour will be discussed later in more detail.

Evidence for red absorption was also found on August 5 (Fig. 5, *right*) but its appearance is more variable with phase. The dominant feature is, however, a strong emission transient that affects mainly the blue wing and the centre of the profile during the first half of the night. This event starts as a dramatic enhancement of the blue wing at $\varphi \simeq$0.5, extending out to –220 km s^{-1}. Its effects are visible in Fig. 3 as a large increase in both EW and FWHM (interval B), with velocities that are significantly blueshifted. Emission moves progressively to the red as the blue wing is seen to fade between phases $0.6 < \varphi <$ 0.8. A dark feature develops at a velocity close to the maximum Doppler blueshift associated to rotational velocity ($\varphi \simeq$0.78)

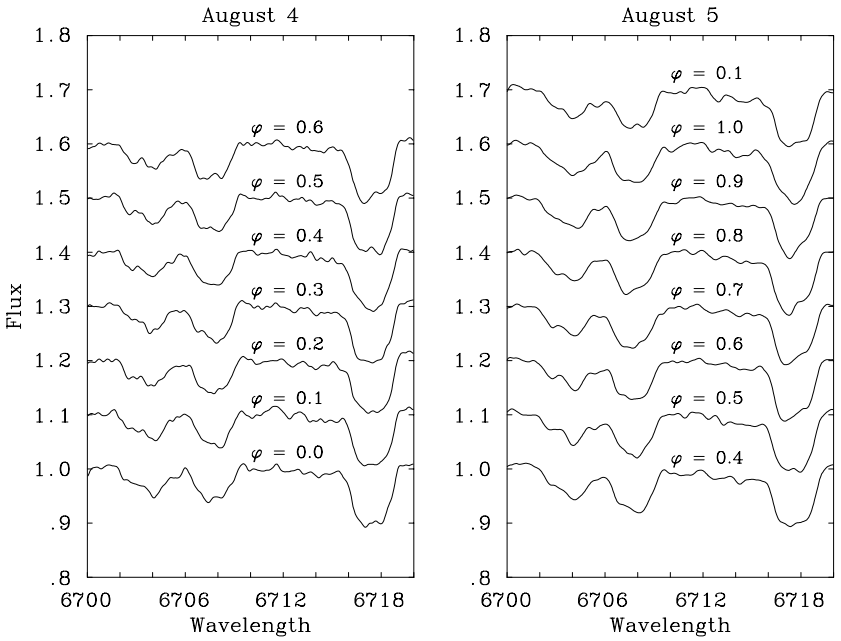

Fig. 6. Sequence of Li I (λ6707 Å) line profiles on August 4 (*left*) and August 5 (*right*). Each profile is an average of four consecutive spectra taken near the phase indicated above it in the plot. Phases were computed according to the period of 10.17 hrs (J94) fixing zero phase at the time of the first exposure on the first night, as in Sect. 4.1

and moves redward until it merges with the absorption feature in the red ($\varphi \simeq 0.95$).

6. The Li I photospheric line

BD+22°4409 has strong Li I λ6708 Å absorption, which, along with other considerations, caused J94 to argue for a youthful evolutionary status. J94 found line profile and EW variations in their data and we have also observed significant changes both between and during the two nights of observation (see Figs. 6 and 7). Fig. 6 shows average line profiles at several epochs. On August 4 (*left panel*) the line depth was smaller with a raised core at phases 0.0, 0.5 and 0.6. On August 5 (*right panel*) there are more noticeable changes in the line asymmetry – the position of maximum absorption appears towards the red at $\phi \simeq 0.5$ and drifts back to the blue at $\phi \simeq 0.8$. The changes in the Li I λ 6708 profiles are followed closely by the nearby Ca I λ 6717 line.

Fig. 7 shows the total EW of the Li λ 6708 feature on August 4 (*open circles*) and 5 (*filled circles*). The error on a single EW measurement is approximately 20 m Å. The EWs show no sign of variation on each night, but there is a significant increase in the mean EW from 142 m Å on August 4 to 215 m Å on August 5. Possibly some of this variation is in the sytematic placement of the continuum, but this could not explain the majority of the difference. The nearby blend of two iron lines at 6704 Å shows an increase in its mean EW from 120 m Å to 145 m Å. Problems with blending of the 6708 Å feature itself are also unlikely to play a part at this spectral resoltuion. The nearby Fe I λ6707.44 Å and Sm II λ 6707.50 Å lines are too weak $<$20 m Å to have much effect. Another possibility is that the largely unknown contribution from molecular opacity might vary in a phase dependent way. There is little overlap in the phase coverage of our observations, although what there is, suggests no phase dependent behaviour. In this situation it is difficult to say whether the EW enhancement on August 5 is a long term effect or perhaps some transient phenomenenon associated with the chromospheric flare activity we observed. Further discussion of the Li variations are given in Sect. 8.4.

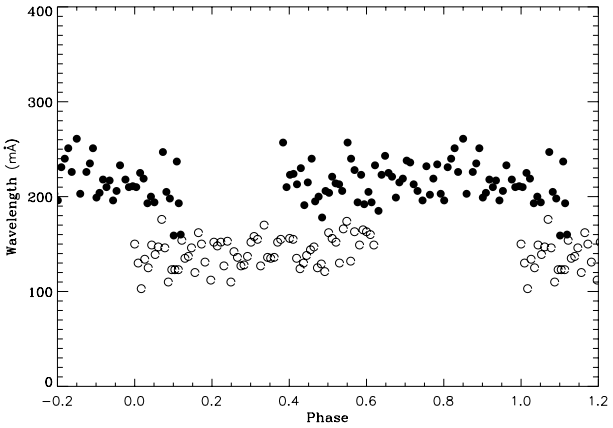

Fig. 7. Time series of the Li I EW on August 4 (*open circles*) and August 5 (*filled circles*. Measurements are very scattered in both nights but it can be seen that the Li I EW is systematically lower on August 4

7. Hα emission features

7.1. Observations on August 4

Evidence of large-scale motions is seen during almost 2 hrs at the beginning of the night ($\varphi \simeq$0–0.16). Fig. 5 (*left*) shows emission out to velocities of $\sim$–250 km s^{-1} implying upward flows of the emitting material. While this is not necessarily a bulk velocity (because the Hα line is optically thick) it probably indicates large upward motion. For comparison, the escape velocity of the star at the surface is $\sim$600 km s^{-1}. Individual line profiles are

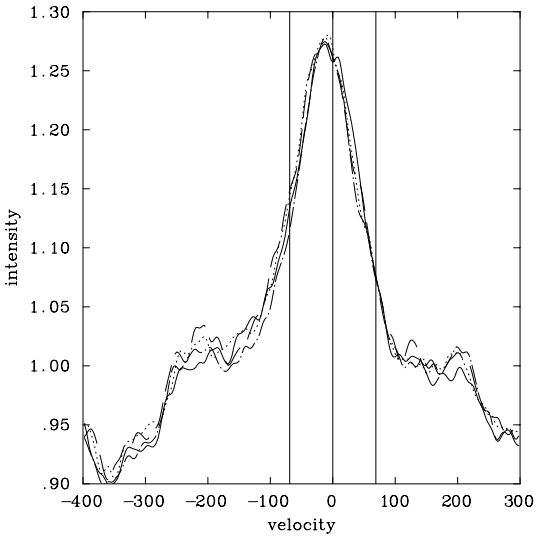

Fig. 8. Sequence of Hα line spectra of BD+22°4409 taken at the beginning of the night August 4 at an interval of ∼7 min, in the order —, – –, ..., –.– from $\varphi \sim 0$ to $\varphi \sim 0.06$. The central line marks the rest velocity of the stellar photosphere and the other two vertical lines indicate the maximum Doppler shifts associated to the rotational velocity, $v\sin i$. Extra emission is clearly seen in the blue wing up to $-200\,\mathrm{km\,s^{-1}}$, away from the line centre. Signs of excess emission are also apparent more or less symmetrically in the red (v∼200 km s^{-1}), as explained in Sect. 7.1

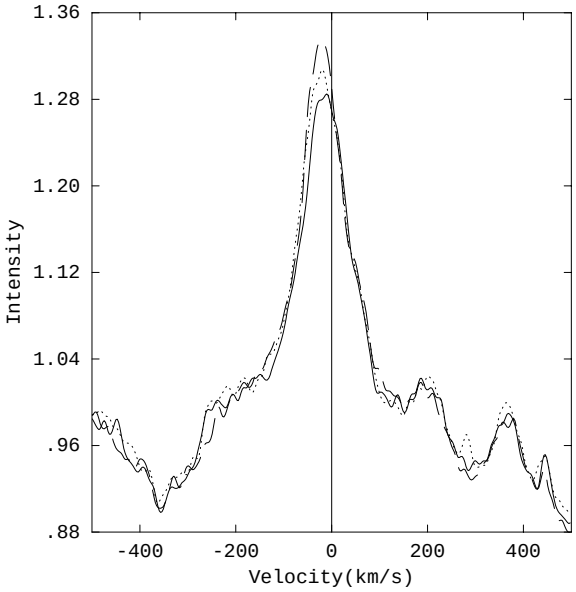

Fig. 9. Series of Hα line profiles illustrating the evolution of the flare seen on August 4. Profiles occur in order of increasing peak, at phases $\varphi \sim 0.11$ (—), $\varphi \sim 0.13$ (...), $\varphi \sim 0.20$ (– –). Note the strong asymmetry in the red wing

displayed in Fig. 8. In order to mark the asymmetry of the profile both two lines are drawn at $\pm 69\,\mathrm{km\,s^{-1}}$, the estimated $v\sin i$ of the star. The intensity of the peak does not exhibit significant changes at those phases, while the red wing is seen to recede slightly. As a result, an overall decrease of both EW and FWHM is observed at these phases in Fig. 3. Note also that changes in the red wing occur mainly at velocities, $v \leq 50\,\mathrm{km\,s^{-1}}$ and that profiles shown are significantly shifted to the blue. This is perhaps the most extreme manifestation of the strong asymmetry presented in Sect. 5 and so confirms that this effect is real rather than just an artifact due to the method of analysis itself.

An emission transient event is seen to start at approx. $\varphi \sim 0.11$ with considerable enhancement of the blue wing of the Hα profile. The phenomenon has been identified as a flare according to the fact that the He I D_3 line went into emission at the time the Hα EW and FWHM reached their respective maxima, $\varphi \sim 0.2$. He I D_3 emission is known as a good indicator for explosive release of energy in connection to flares. However, contrary to what is commonly seen during flares there is no appreciable change in the red wing of the Hα line profile, and so the asymmetry we referred to before becomes more evident at these phases. The flare corresponds to the well distinguished peaks in both EW and FWHM that are shown in Fig. 3 (intervals B–C), at the time of maximum blueshift. This is illustrated by the sequence of profiles in Fig. 9. The line wings extend to much larger velocities on the blue side than on the red side.

Extra emission reappears weakly in the far blue wing ($v\sin i \sim$–240 km s^{-1}) at $\varphi \simeq 0.34$ on a short time scale (≃40 min). This feature is presumably due to less intense mass motions. Another possibility is that it results from the scattering of light by co-rotating clouds back into the line of sight. In this case, the observed velocities imply a projected cloud distance of $\sim 3.6 R_* \sin i$ ($v = \Omega R$), which may be compared to the stellar co-rotation radius, $R_{corot} = 2.83 R_*$. Evidence of a pedestal emission, that could be interpreted as the signature of co-rotating clouds is also clear in Fig. 8, is detected symmetrically in the far wings of the Hα profile ($v \sim \pm 200\,\mathrm{km\,s^{-1}}$).

Evidence of excess emission in the blue wing is found again at the end of the night ($\varphi \simeq 0.58$–0.62) with velocities in the order of –200 km s^{-1}. This occurs at the time the Hα line is stronger and more symmetric, showing a weaker red-shifted absorption than during the rest of the night.

7.2. Observations on August 5

During this night the star displays a higher level of activity than in the previous night. The series of spectra shown in Fig. 10 were selected to illustrate the evolution of the Hα line profile during the main period of activity. This consisted of two contiguous episodes, within which the line was seen to enhance progressively and decay afterwards in a continuous way. Therefore, the whole sequence is segmented in four different sets of successive spectra, each of them corresponding to a monotonic increase/decrease of the Hα emission. Spectra in the same set are overplotted using different line styles. In order to help to follow the relative changes in the profile, the last spectrum of each set is also the first one in the next set. The two vertical lines mark the velocity range $\pm v sin i$ and the corresponding phases are annotated in the right to allow comparison with Fig. 3.

A first brightening with simultaneous fast ejections of material was already developing when the observations started.

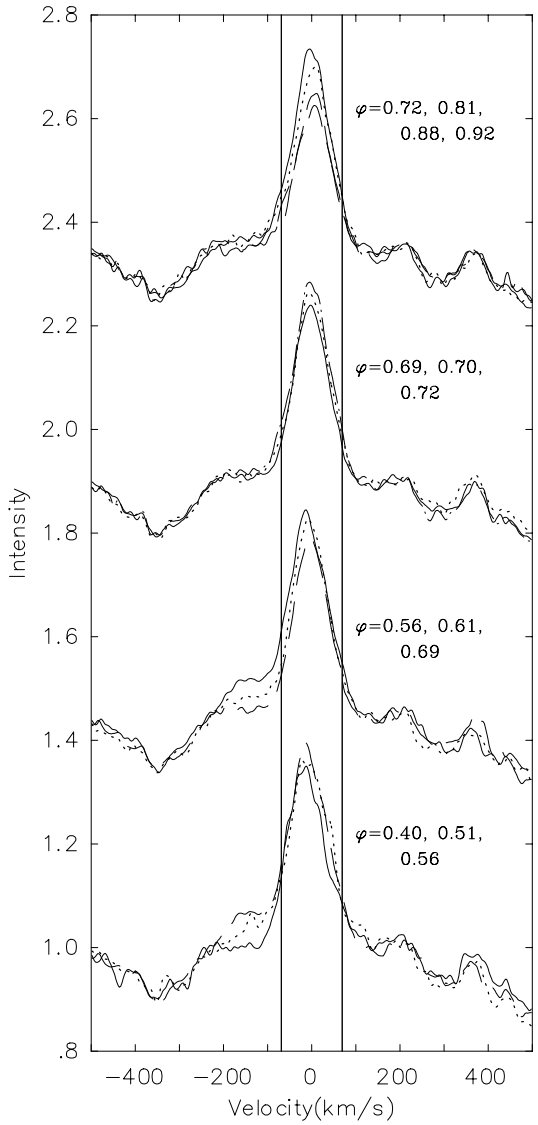

Fig. 10. Series of Hα line profiles illustrating the evolution of the large flare seen on August 5. The spectra are grouped in different sets to represent the main stages of the whole event, as discussed in Sect. 7.2. Different line styles were used to distinguish them. The last spectra of each set (– –) is always the first one in the next set (—) and the corresponding phases are written on the right. While profiles in the first and third sets (from bottom to top) are in order of increasing line peak, in the second and fourth sets of profiles are in order of decreasing peak

Note the extra emission seen in Fig. 10 at velocities up to $v \sim$-200 km s^{-1} as the flare evolves. The Hα line becomes gradually more symmetric and considerably stronger, up to an absolute maximum EW $\simeq$0.97, reached at both $\varphi \simeq$0.48 and $\varphi \simeq$0.57. A considerable blueshift becomes evident at this time in spite of the fact that the Hα line seems to be inherently drifting to the red during the whole interval of phases $\varphi \simeq$0.4-0.9 (see Fig. 3). Such discontinuity is actually due to significant mass motions in the blue together with an absorption of the red wing that causes a strong asymmetry in the profile (see Figs. 5 (*right*) and 10). This is the same absorption effect that was observed during the previous night but it is less important here and does not persist during the flare. A simple blueshift of the line centre would not explain the extreme asymmetry of the profile and would also be difficult to understand since the Doppler shift of the line tends to be positive at these phases according to the observed modulation of the RV parameter.

He I D_3 emission was also detected during the steep rise of the Hα EW curve in Fig. 3. This feature, together with a dramatic enhancement of the Balmer lines, are both characteristic of the solar flare spectrum. Thus, the phenomenon seen here is ascribed to a chromospheric flare in BD+22°4409.

The decay of the flare corresponds to the second set of spectra in Fig. 10, at phases $\varphi \simeq$0.56-0.70, and leads to very low values of EW and FWHM ($\varphi \sim$0.7). Apparently it consists of a progressive absorption in the blue wing with respect to the preceding spectra but this could be caused by the intrinsic modulation of the line as manifested by the temporal evolution of the RV parameter in Fig. 3.

A similar phenomenon follows at $\varphi \simeq$0.72, with associated He I D_3 emission. As before, this second event is attributed to another flare. The corresponding profiles in Fig. 10 show the rapid rising of the flare and its posterior decay. However, its effects are only important in the core of the line and there is no sign of extra emission in the wings. It extends over a shorter interval of phases, corresponding to the narrower peaks of both EW and FWHM that follow the previous flare in Fig. 3. Note that the FWHM does not experiment such a large increase as the EW does, reflecting the fact that this second brightening enhances mainly the peak of the line.

In contrast with the first flare, this second event decays rapidly just after the time of the maximum at $\varphi \simeq$0.8. The EW and FWHM of the line decrease dramatically as the left half of the profile is seen to recede. An absolute minimum of emission is reached at $\varphi \simeq$0.92 before the line recovers again. At these phases rotational modulation effects could not be significantly affecting the appearance of the profile as the line centre keeps at velocities close to zero. The strong depression seen in the blue wing while the peak velocity does not shift significantly to the red argues for a real absorption component observed at negative velocities (v$\simeq$–50 km s^{-1}). A preflare spectrum is not available due to the complexity of the whole flare event and also because when the observations started the first part of the flare was already in progress. Therefore, an attempt to remove the rotational modulation effects and study in more detailed the intrinsic flare emission would be inappropriate.

8. Discussion

8.1. General variability of the chromospheric emission

A quantitative analysis of the Hα and Hβ line profiles was presented in Sects. 4.1 and 4.2. At first glance the RV variations might suggest rotational modulation of active regions responsible for the chromospheric emission. This idea would be also supported by the sinusoidal variations of the star's radial velocity, RV$_{phot}$ (see Sect. 3.1). From Figs. 1, 3 and 4 it is seen that

variations in radial velocity for the chromospheric Balmer lines are anticorrelated with variations in RV_{phot} measured from photospheric lines. This would be expected to be observed if those variations were due to active regions consisting of photospheric spots with overlying plages. A spot approaching the receding limb would cause a blueshift in photospheric lines while, in contrast, the overlying plage would show itself as excess red-shifted emission in the chromospheric lines. The fact that a correlation is seen between the Hα and Hβ lines, both showing anticorrelation with photospheric lines, argues strongly for active regions. However, there are some problems related to this interpretation. First, the RV_{phot} modulation observed in the photospheric lines is weaker on August 4. It is possible that significant changes in the pattern of active regions are responsible for the different behaviour of RV_{phot} in the second night, when strong flare activity has also been detected (see Sect. 7.2). Observational evidence in support of the association of strong flares with light curve changes have been found in active binary systems. Catalano & Frasca (1994) detected a large flare in the active RS CVn star HK Lac, and discussed its connection to the development of a new spot group in the stellar surface. More examples in other RS CVn systems can be found in Teriaca (1997). Also, it is well known that large flares are often triggered by the interaction between old and new magnetic structures in the solar case (Gaizauskas 1989).

Second, although there is a correlation between the RV variations seen in Hα and Hβ, rotational modulation effects appear to be more firmly established in the case of Hβ, since its RV curve has a larger amplitude and varies more symmetrically with respect to zero velocities. This is more difficult to explain in terms of active regions only.

Finally, the FWHM and EW of the Balmer lines do not show the same gradual trend seen in RV. In contrast, they are seen to undergo more irregular variations although, in general, the EW curves indicate that the chromosphere brightness becomes greater at $\varphi \simeq 0.5$, coinciding with two consecutive flare brightenings at the night of August 5.

It is clear that rotation of surface active regions cannot explain by itself the variability of the chromospheric emission. There are other important sources of variability. One is the strong absorption seen almost permanently in the red on the two nights but with higher contrast on August 4. This feature explains the permanent displacement of the Hα line towards the blue. In addition, because its strength is not uniform with phase (see Sect. 5), it may be also related to the RV modulation. In this case, however, better agreement would be expected between Hα and Hβ observations. This and other aspects concerning the absorption features are discussed separately (see Sect. 8.3). Additional variations are due to transient flaring, particularly noticeable in EW and FWHM. However, these are seen as deviations from the general trend and would not cause any phased modulation. In general, flares are less well defined in the Hβ EW and FWHM curves, which may explain some of the differences observed in the behaviour of this line with respect to that of Hα. Flaring is discussed in more detail below.

8.2. Flaring activity

The assignment of the observed emission transients to flares is supported by the D_3 emission seen at those phases when Hα is strongest, which is one of the invariable features in the solar flare spectrum during the flash phase (Švestka 1976). Maximum flaring is displayed on the second night, when two consecutive flares were seen to occur in association with relevant phenomena we discuss next.

The strong enhancement of the blue wing of the Hα line during flares is explained in the context of flare dynamical models as an indicator of chromospheric evaporation. Excess emission at velocities between –150 and –200 km s^{-1} is observed as part of the flaring in the two nights, suggesting fast ejections of hot material. Considering initial velocities of that order the maximum height that is expected to be reached by the ejected gas if following a radial trajectory under gravity is about 33000 km, which is comparable to the typical loop heights in solar flares. However, the upflow would only last about 7 min. The fact that the extra emission in the blue is clearly visible at least during 2 hr in the second night suggests ejection is taking place continuously, in which case it could constitute a powerful supply of prominence material.

Fast and sporadic injections of chromospheric material are believed to contribute to the total mass of solar prominences. However, the mass required to maintain them cannot be supplied only by this source. At present, several models have been developed to study possible injection mechanisms that can account for prominence formation, involving macroscopic and microscopic flows of material. Among the most efficient macroscopic processes stands evaporation (Poland & Mariska, 1986), with corresponding upflows in the range of 100-500 km s^{-1}, and ballistic injections of matter (An et al., 1988a, b; Wu et al. 1990), with initial velocities not exceeding 20 km s^{-1}. However, loop prominences are known to be associated with energetic flares producing a large amount of fast particles. The prominence formation model due to Jefferies & Orrall (1965) consider that some of these fast particles travel up into the loop and remain stored in the magnetic field, thus providing the required mass and energy to form the prominence.

The behaviour of the Hα line during the decay of the second flare event observed at the night of August 5 differs remarkably from the standard. The distinct feature is a strong absorption seen at velocities v $\sim$–50 km s^{-1} as explained in Sect. 7.2. A similar phenomenon is sometimes observed after the maximum of large solar flares, owing to cool dark loops that are seen in absorption against the flare background. The loops system appears to rise at a rate of $\sim$5-10 km s^{-1}, as new loops form at larger heights while the old, lower ones, fade away. In the stellar case we do not have the spatial resolution to detect them. However, our result may provide indirect evidence for analogous forms of activity.

8.3. Nature of the Hα profile asymmetry

The fact that the observed Hα profile is very asymmetric, as well as narrower than expected given the calculated rotational veloc-

ity, has been proved to be due to a strong absorption at positive velocities. This would admit two possible interpretations.

First, it can be understood in terms of material falling down into the chromosphere under the effect of gravity, in a way reminiscing the coronal rain phenomenon.The same particle-acceleration mechanism used in Jefferies and Orrall's model was proposed by the authors to explain the origin of coronal rain from the ejected particles stored in the magnetic field of the inner corona. Additionally, coronal rain is in some cases the remnant of precedent flare loops in the Sun.

The other possible interpretation is as an intense and continuous downflow of material along magnetic loops, by analogy with which is typically observed in solar loop prominences (Tandberg-Hanssen, 1995). In fact, both phenomena, coronal rain and downflows in loop prominences, are normally very difficult to distinguish, even in the case of the Sun, where the spectral resolution allows to measure real velocities.

On a rapidly-rotating star like BD+22°4409, a strong downflow of cool absorbing material can be produced as a result of the interaction between the magnetic field and the stellar plasma in conditions of unstable mechanical equilibrium. This is explained in the context of prominence clouds formation and stability in late-type rapid rotators, according to a previous study of the mechanical forces acting on the neutral material that is tied to the magnetic field above the chromosphere (van den Oord et al. 1998). At the typical heights where the clouds are found the effective component of the magnetic field is the dipole component, and mechanical equilibrium on a field line is possible only in the equatorial plane. Under this assumption, the study demonstrates that for heights lower than a certain limit the neutral material suspended in the magnetic field is in unstable equilibrium and may fall back into the chromosphere along the field lines. Prominences may exist at larger heights in the equatorial plane, where stable equilibrium is possible. However, they would be impossible to detect in projection on the stellar disk due to the inclination of the stellar rotation axis, $i \sim 50°$. In this case they would never result in absorption transients.

A downflow of cool material towards the stellar poles is not predicted by previous works on formation and stability of prominences in rapidly-rotating stars. Collier-Cameron (1988) developed a model to explain the formation of prominences as condensation in loops that extend beyond the co-rotation radius, where the effective gravity is directed towards the star. Ferreira & Jardine (1995) addressed the stability of filament-like structures in rapidly-rotating stars by considering a ring-like filament current around the stellar equator. In that scenario there is no connection between the filament field and the photosphere, in which case it would be difficult to argue for a downflow of material in any preferred direction.

Our results suggest that prominence phenomena may manifest in other ways than just as systematic variations in the fluxes. Therefore, the investigation of mass flows and asymmetric profiles may provide a way, perhaps unique, to detect prominence activity in other stars, specially in those where we have no spatial resolution, i.e. all non-rapid rotators. Evidence of asymmetries in the profiles of active late-type stars has increased considerably in the last few years. Byrne et al. (1995) has convincingly demonstrated a strong asymmetry in the Hα emission profile of the active RS CVn-type star II Peg (see also Byrne et al. 1997). Similar to the case of BD+22° 4409, the Hα emission in II Peg is mainly seen in the blue. The same asymmetry seems to occur also in the central reversal and can be observed in other lines, like He I 10830 Å(Byrne et al. 1997). If this effect can be interpreted as due to mass infall and it is detected in a large number of stars, it may indicate that prominences are an important component of the stellar atmospheres.

8.4. Lithium and effects of spot activity

The Li I line is very strong and shows significant variations in equivalent width and profile shape. Small variations have been previously observed by J94 at lower spectral resolution. An explanation based on large spotted regions which move across the stellar surface was suggested by those authors. The existence of spots was supported by the light modulation and the observed sinusoidal variations of the stellar radial velocity. The higher spectral resolution of the present observations has allowed to unequivocally detect the effect of surface spots on the temperature-sensitive Li I line. Systematic profile changes were seen to correlate with variations in profile shape seen in other spot-sensitive lines (Ca I λ6717 Å and Ca I λ6439 Å). This also explains the apparent modulation of RV_{phot} (see Sect. 3.1), as suggested in J94.

These kinds of effects are seen most clearly in the second night of observations. On August 4 the variability of the line profile is not so extreme and the amplitude of the RV_{phot} variations is generally smaller. In addition, the Li I EW is systematically lower. Possible variations due to the overlying molecular absorption in the Li I spectral region have been suggested (see Sect. 6) but that would not explain the different behaviour of RV_{phot} in both nights. The difference in phase coverage may be important and future observations are required to resolve this. Moreover, two consecutive flares were observed on August 5 (see Sect. 7.2) which are presumably connected to changes in spot configuration, as suggested in Sect. 8.1. If such was the case, variations in Li I EW could be a manifestation of stronger spot activity. Because the density of neutral lithium increases at lower temperatures, Li is expected to be enhanced in spotted regions. Therefore, Doppler imaging analysis of BD+22°4409 are very important to clarify this point.

According to previous results obtained by Pallavicini et al. (1993), no significant variations of the Li I line are to be expected in spotted stars. However, evidence of Li I variability, presumably associated to spot activity, has been reported in other stars (Fernández & Miranda 1998, Martín & Claret 1996). Results from future observations of BD+22°4409 promise valuable information in this respect.

9. Conclusions

BD+22°4409 is a magnetically active and rapidly-rotating late-type star. A considerable degree of activity in the form of flares

and plage regions has been detected in our observations in accordance with previous work by J94. The analysis of photospheric lines has revealed the presence of large spots.

Evidence of an intense downflow of material has also been shown in this paper. Its origin has been discussed in terms of coronal rain and loop prominences phenomena. Based on a recent analysis of the equilibrium and stability of prominence-like cloud in late-type rotators (van den Oord et al. 1997), we conclude that the intense downflow of cool absorbing material is more likely to derive from the interaction between the magnetic field and the stellar plasma in conditions of unstable mechanical equilibrium, thus resembling the loop prominences phenomenon.

Taking into account the results from observations made so far it seems that the loop prominence systems are a common feature in the star BD+22°4409. The possibility of condensations as in the case of HK Aqr or AB Dor cannot be ruled out, although a definitive observational proof may be impossible to obtain due to geometrical considerations.

More extended observations are needed to discriminate better between transient phenomena and long-term variations. It would also be interesting to investigate the possible connection of the photospheric variability to chromospheric emission variability.

Acknowledgements. Research at Armagh Observatory is grant-aided by the Department of Education for Northern Ireland. We would like to thank the support staff of the WHT (La Palma) for their assistance during the observations. We also acknowledge the support provided by the STARLINK project funded by the UK PPARC. MTE was supported by a PPARC Research Studentship No. 9400747X during the period 1994–1997. MTE thanks all the staff in LAEFF for their kind support during the last steps of this work, particularly Dr. B. Montesinos for his help and careful reading of the manuscript.

References

An C.-H., Bao J.J., Wu S.T., 1988a, Solar Phys. 115, 81
An C.-H., Bao J.J., Wu S.T., Suess S.T., 1988b, Solar Phys. 115, 93
Bodenheimer P., 1965, ApJ 142, 451
Basri G., Martin E.L., Bertout C., 1991, ApJ 341, 340
Bromage G.E., 1984, Proc. 4th European IUE Conf., ESA SP-218, p. 473
Byrne P.B., Eibe M.T., Rolleston W.R.J., 1996, A&A 311, 651
Byrne P.B., Eibe M.T., van den Oord G.H.J., 1997, In: Webb, Rust D., Schmeider B. (eds.) New Perspectives on Solar Prominences. Proc. IAU Coll. 167, Astron. Soc. of the Pacific Conference Series, San Francisco, CA, 1998
Byrne P.B., Sarro L.M., Lanzafame A.C., 1997, In: Bookbinder J., Donohue R. (eds.) Cool Stars, Stellar Systems and the Sun. ASP Conf. Ser., in press
Byrne P.B., Panagi P.M., Lanzafame A.C., et al., 1995, A&A 299, 115
Cameron A.C., Robinson R., 1989a, MNRAS 236, 57
Cameron A.C., Robinson R., 1989b, MNRAS 238, 657
Collier-Cameron A., 1988, MNRAS 233, 235
Collier-Cameron A., Woods J.A., 1992, MNRAS 258, 360
Catalano S., Frasca A., 1994, A&A 287, 575
D'Antona F., Mazzitelli L., 1984, A&A 138, 431
Duncan D.K., 1981, ApJ 248, 651
Eibe M.T., 1998, A&A, 337, 757
Fernández M., Miranda L.F., 1998, A&A 332, 629
Ferreira J.M.T.S., Jardine M., 1995, A&A 298, 172
Gaizauskas V., 1989, In: Haisch B., Rodonò M. (eds.) Solar and Stellar Flares. Kluwer Academic Publishers, Dordrecht, p. 135
Gunn A.G., Doyle J.G., 1997, A&A 318, 60
Gunn A.G., Doyle J.G., Houdebine E.R., 1997, A&A 319, 211
Hall J.C., Ramsey L.W., 1992, AJ 104, 1942
Hobbs L.M., Pilachowski C., 1988, ApJ 334, 734
Jefferies J.T., Orrall F.Q., 1965, ApJ 141, 519
Jeffries R.D., 1993, MNRAS 262, 369
Jeffries R.D., Byrne P.B., Doyle J.G., et al., 1994, MNRAS 270, 153 (J94)
Martín E.L., Claret A., 1996, A&A 306, 408
Pallavicini R., Cutispoto G., Randich S., Gratton R., 1993, A&A 267, 145
Pinnsoneault M.H., Deliyannis C.P., Demarque P., 1990, ApJS 78, 179
Poland A.I., Mariska J.T., 1986, Solar Phys. 104, 303
Skumanich A., 1972, ApJ 171, 565
Soderblom D.R., Stauffer J.R., MacGregor K.B., Jones B.F., 1993, ApJ 409, 624
Stauffer J.R., Soderblom D.R., 1991, In: The Sun in time. University of Arizona Press, Tucson, AZ, p. 832
Stauffer J.R., Hartmann L., Soderblom D.R., Burnham N., 1984, ApJ 280, 202
Stauffer J.R., Hartmann L., Burnham N., Jones B.F., 1985, ApJ 289, 247
Strom K.M., Wilkin F.P., Strom S.E., Seaman S.L., 1989, AJ 98, 1444
Ŝvestka Z., 1976, Solar Flares. D. Reidel Publ. Co., Dordrecht
Tandberg-Hanssen E., 1995, Solar Prominences. D. Reidel Publ. Co., Dordrecht
Teriaca L., 1997, In: Stellar Flare and Light Curve Variations in Active Binary Systems. Degree-thesis in Physics, Catania University
Tody D., et al., 1986, IRAF User's Manual. National Optical Astronomical Observatories
Unger S., Pettini M., 1993, UES User's Manual. Isaac Newton Group, La Palma
van den Oord G.H.J., Eibe M.T., Byrne P.B., 1997, A&A, submitted
Wu S.T., Bao J.J., An C.-H., Tandberg-Hanssen E., 1990, Solar Phys. 125, 277